Durham University

Durham Research Online

Deposited in DRO:

11 May 2017

Version of attached file:

Accepted Version

Peer-review status of attached file:

Peer-reviewed

Citation for published item:

Wyper, Peter F. and Antiochos, Spiro K. and DeVore, C. Richard (2017) 'A universal model for solar eruptions.', Nature., 544 (7651). pp. 452-455.

Further information on publisher's website:

https://doi.org/10.1038/nature22050

Publisher's copyright statement:

Additional information:

Use policy

The full-text may be used and/or reproduced, and given to third parties in any format or medium, without prior permission or charge, for personal research or study, educational, or not-for-profit purposes provided that:

- a full bibliographic reference is made to the original source
- a link is made to the metadata record in DRO
- the full-text is not changed in any way

The full-text must not be sold in any format or medium without the formal permission of the copyright holders.

Please consult the full DRO policy for further details.

Durham University Library, Stockton Road, Durham DH1 3LY, United Kingdom
Tel : +44 (0)191 334 3042 | Fax : +44 (0)191 334 2971
https://dro.dur.ac.uk

A Universal Model for Solar Eruptions

Peter F. Wyper[1], Spiro K. Antiochos[2], & C. Richard DeVore[2]

1. Department of Mathematical Sciences, Durham University, Durham, DH1 3LE, UK.

2. Heliophysics Science Division, NASA Goddard Space Flight Center, 8800 Greenbelt Rd, Greenbelt, MD 20771, USA.

Magnetically driven eruptions on the Sun, from global-scale coronal mass ejections[1] (CMEs) to small-scale coronal X-ray and Extreme Ultraviolet (EUV) jets[2-4], have frequently been observed to involve the ejection of the highly-stressed magnetic flux of a filament[5-9]. In fact, it was recently concluded from new observations that all coronal jets are driven by filament ejection, just like large CMEs[10]. Theoretically, however, CMEs and coronal jets have been thought to arise through very different mechanisms: with CMEs from an "ideal" process, whereby the energy release does not require a change in the magnetic topology, as in the kink or torus instability[11,12]; and coronal jets from a resistive process[2,13] involving magnetic reconnection. The observations challenge this understanding and suggest that a single mechanism may be responsible, i.e., either CMEs arise from reconnection, or jets from an ideal instability. Here we report simulations of coronal jets driven by "filament channel ejection", whereby a region of highly sheared magnetic field near the solar surface becomes unstable and erupts. The results show definitively that reconnection drives the jet. We conclude from our calculations that if CMEs and coronal jets are indeed physically identical then reconnection also drives coronal mass ejections.

To test quantitatively the hypothesis that coronal jets are in fact miniature versions of coronal mass ejections, we performed an ultra-high-resolution 3D simulation that captures as closely as possible the salient features of a coronal jet magnetic system containing a so-called "mini-filament"[10,14]; a miniature version of the large-scale filaments that form in filament channels and erupt as coronal mass ejections. This is the highest-resolution adaptive-mesh calculation of its type to date, and it clearly resolves for the first time different stages of the mini-CME jet. The setup is similar to our previous calculations[15,16] (see methods section for details). To represent an emerged bipolar region in a solar coronal hole, we start with a strong bipole embedded in an inclined, uniform, ambient field (Figure 1a). This configuration naturally creates the loop field structure (sometimes called the anemone region)[17] observed at the base of coronal jets, with a domed separatrix surface and 3D null point at the boundary between the open- and closed-field regions. The initial system is current-free and, therefore, has no filament and no free energy to power an eruption. We energize the system and create the filament by shearing the footpoints of field lines connecting to the parasitic (positive) polarity over a finite time interval. The driving is subsonic and sub-Alfvénic so that the shear is built up quasi-statically, and the driving is localized to a narrow region about the polarity inversion line so that a filament-channel-like structure develops. This shearing is merely a numerically convenient way to inject free energy into the field near the polarity inversion line (PIL), where we know the energy must be stored due to the positioning of the mini-filament. The driving could represent energy injection/storage at the PIL via very slow flux emergence or cancellation, photospheric shearing motions, or helicity condensation[18] (the cumulative effect of quasi-random surface

motions). We end the slow footpoint shearing well before any evidence of jetting activity in our simulation. Consequently, the shearing serves only to provide free energy to the system; it does not directly drive the resulting explosion.

Figure 2a shows the strongly sheared magnetic field (yellow) created by the end of the driving period. Such a field structure is observed to support cool, dense plasma against gravity in large-scale filaments[19] and is expected to exist within the mini-filaments involved in coronal jets. Restraining field (magenta) overlying the filament pins it down near the photosphere. The key to whether the filament will erupt is whether it can overcome this restraining field.

The breakout model for large-scale CMEs[20,21] offers a natural avenue for this to occur. It asserts that when magnetic shear is added at the PIL of an arcade beneath a coronal null point (Figure 3a-b), the overlying restraining field must expand upward and create a current sheet at the null point. Reconnection at this sheet then slowly removes the restraining field. Beyond a critical threshold, a feedback (breakout) process is initiated whereby the removal of restraining field leads to a runaway upward expansion of the sheared field[20]. This expansion stretches the sheared field to the point that another current sheet with further magnetic reconnection is initiated beneath the erupting field (Figure 3c-d), forming and expelling the CME flux rope and generating the intense flare loops[21].

We find a similar evolution in our "breakout jet" configuration, Figure 1 (see also Supplementary Video 1). As the strongly sheared field builds up along the PIL between the flux concentrations of the bipole, the restraining field (blue) expands upwards towards the null (Figure 1b). This creates the breakout current sheet that reconnects the restraining field to the other side of the null dome and to the open field (Figure 1b-c). Thus, the breakout reconnection removes restraining field and also produces a slow, tapered outflow of plasma. As the filament field continues to expand, slow internal reconnection turns the sheared-field region into a twisted flux rope, the structure required for kink or torus instability[11,12]. Continued breakout reconnection slowly lifts the flux rope towards the breakout current sheet. The rise speed of the flux rope increases from around 10 km s^{-1} to 40 km s^{-1} during this phase (Extended Data Figure 1), agreeing with the observed values and explaining the slow-rise phase of mini-filaments in coronal jets[10] (Figure 1b-c). The key result is that little energy is released during this time, as expected for the breakout process[21] (Figure 4). *Explosive energy release occurs only when the flux rope reaches the breakout sheet and reconnects onto the open field.* In our simulation, the eruption is clearly due to a resistive process – reconnection – not to an ideal process.

The rapid reconnection between the twisted flux rope and the background open field launches an untwisting jet along the ambient open field, whilst simultaneously stretching out the sheared field to initiate flare reconnection and form the flare loops (Figure 1d). The jet itself is a combination of a nonlinear torsional Alfvén wave and the Alfvénic outflow emanating from the flare current sheet. The torsional wave component is launched when the twist within the flux rope begins to spread along the ambient open field, following reconnection at the breakout current sheet. Magnetic tension around the periphery and at the nose of the expanding flux rope accelerates plasma within the flux rope (the core of which formed the filament) into a rotating spire. A component of this untwisting wave also drives part of the flux-rope plasma

upwards as the wave propagates[22]. Rotational and upward velocities within the jet spire approach the local Alfvén speed of around 300 km s^{-1}. Coupled to this are the fast outflows from the flare current sheet, which act to strengthen the rotation and the vertical component of the untwisting wave. This combination of hot jet outflow mixed with cool filament material ejected at a few hundred km s^{-1} is exactly what is observed in mini-filament coronal jets[10,14].

Figure 2b shows the 3D shape of the jet (see also Supplementary Video 2). The untwisting spire arising from one side of the jet base, opposite the flare loops formed on the other, explains the separation of the spire and compact bright point, respectively, in the observed jets. An example of such an observed mini-filament jet[23] is shown in Extended Data Figure 2 (see also Supplementary Video 3). The tapered outflow arising from the sharp interface above the mini-filament in Extended Figure 2a and the slight brightening of the right-side loop structure are explained by the positioning of the breakout current sheet and the weak reconnection outflows that we see in our simulation prior to onset of the eruptive jet.

Figure 3 illustrates how the main stages of our breakout jet compare with large-scale breakout CMEs. The critical physical difference between the two configurations is the role of expansion. In CMEs, the complete erupting system – flux rope and overlying field – can expand to many times its original size as is evident in Figure 3c-d. This purely ideal expansion, by itself, produces a large energy decrease. The reconnection that is evident in Figure 3c-d could well be a by-product of the ideal expansion, rather than the driver of the expansion. In CMEs, therefore, it is difficult, with either observations or simulations, to separate the effects of the ideal and resistive processes and determine definitely the mechanism for eruption. By contrast, in coronal jets the background field is strong and drops off negligibly with height over the scale of the jet region, so the ideal expansion is completely suppressed. The closed-field region in our simulation simply lacks sufficient free energy to push aside the surrounding field and open ideally. We note that in Figure 3e-h the closed-field region expands only marginally throughout the event. In our simulation, the sharp increase in kinetic energy and the explosive jet are due solely to a rapid increase in reconnection at the breakout current sheet.

Our results yield two far-reaching conclusions. First, the breakout mechanism is universal across multiple scales in the Sun's corona, occurring wherever free magnetic energy builds up at a PIL. Consequently, our model can explain CME-like eruptions that occur from large[1] to small[6,7,9] scales, including those associated with jets[10]. The strength of the overlying field and the closed or open nature of this field dictate the appearance of the eruption, with large-scale CMEs and breakout jets at opposite ends of a spectrum that also includes confined flares and failed filament eruptions[24] and may even extend to explosive events at still smaller scales, such as chromospheric jets[25], spicules[26], and Ellerman bombs[27,28]. Second, the runaway reconnection mechanism of the breakout model, which is inherently a resistive process, is all that is required for explosive eruption. Unlike numerical simulations of large CMEs, in which it is difficult to separate the effects of reconnection from ideal expansion, ideal processes play no substantial role in jets. Therefore, our results demonstrate that if coronal jets and CMEs are physically identical in origin, resistive reconnection is paramount.

References

1. Webb, D. F. & Howard, T. A. Coronal mass ejections: observations. *Living Rev. Sol. Phys.* **9**, 3 (2012).
2. Shibata, K. *et al.* Observations of x-ray jets with the Yohkoh soft x-ray telescope. *Publ. Astron. Soc. Jpn.* **44**, L173-L179 (1992).
3. Shimojo, M. *et al.* Statistical study of solar x-ray jets observed with the Yohko soft x-ray telescope, *Publ. Astron. Soc. Jpn.* **48**, 123-126 (1996).
4. Savcheva, A. *et al.* A study of polar jet parameters based on Hinode XRT observations. *Publ. Astron. Soc. Jpn.* **59**, S771-S778 (2007).
5. Shibatta, K. Evidence of magnetic reconnection in solar flares and a unified model of flares. *Astrophys. Space Sci.* **264** 129-144 (1999).
6. Innes, D. E., Genetelli, A., Attie, R., & Potts, H. E. Quiet Sun mini-coronal mass ejections activated by supergranular flows, *Astron*. *Astrophys*. **495**, 319-323 (2009).
7. Innes, D. E., McIntosh, S. W., & Pietarila, A. STEREO quadrature observations of coronal dimming at the onset of mini-CMEs, *Astron*. *Astrophys*. **517**, L7 (2010).
8. Raouafi, N. -E., Georgoulis, M. K., Rust, D. M. & Bernasconi, P. N. Micro-sigmoids as proginators of coronal jets: is eruptive activity self-similary multi-scaled? *Astrophys. J.* **718**, 981-987 (2010).
9. Schrijver, C. J. Eruptions from solar ephemeral regions as an extension of the size distribution of coronal mass ejections, *Astrophys*. *J*. **710**, 1480-1485 (2010).
10. Sterling, A. C., Moore, R. L., Falconer, D. A. & Adams, M. Small-scale filament eruptions as the driver of X-ray jets in solar coronal holes. *Nature* **523**, 437-U130 (2015).
11. Török, T. & Kliem, B. Confined and ejective eruptions of kink-unstable flux ropes, *Astrophys. J. Lett.* **630**, L97-L100 (2005).
12. Kliem, B. & Török, T. Torus instability. *Phys. Rev. Lett.* **96**, 255002 (2006).
13. Yokoyama, T. & Shibata, K. Magnetic reconnection as the origin of x-ray jets and Hα surges on the sun, *Nature* **375**, 42-44 (1995)
14. Zhang, Q. M. *et al.* Explosive chromospheric evaporation in a circular-ribbon flare, *Astrophys. J. Lett.* **827**, 27 (2016).
15. Pariat, E., Antiochos, S. K. & DeVore, C. R. A model for solar polar jets. *Astrophys. J.* **691**, 61-74 (2009).
16. Wyper, P. F., DeVore, C. R., Karpen, J. T. & Lynch, B. J. Three-dimensional simulations of tearing and intermittency in coronal jets. *Astrophys. J.* **827**, 4 (2016).
17. Nishizuka, N. *et al.* Giant chromospheric anemone jet observed with Hinode and comparison with magnetohydrodynamic simulations: Evidence of propagating Alfvén waves and magnetic reconnection. *Astrophys. J.* **683**, L83-L86 (2008).
18. Antiochos, S. K. Helicity condensation as the origin of coronal and solar wind structure. *Astrophys. J.* **772**, 72 (2013).
19. Martin, S. Conditions for the formation and maintenance of filaments, *Sol. Phys.* **182**, 107-137 (1998)
20. Antiochos, S. K., DeVore, C. R. & Klimchuk, J. A. A model for solar coronal mass ejections. *Astrophys. J.* **510**, 485-493 (1999).

21. Karpen, J. T., Antiochos, S. K. & DeVore, C. R. The mechanisms for the onset and explosive eruption of coronal mass ejections and eruptive flares. *Astrophys. J.* **760**, 81 (2012).
22. Shibata, K. & Uchida, Y. Sweeping-magnetic-twist mechanism for the acceleration of jets in the solar atmosphere. *Sol. Phys.* **103**, 299-310 (1986).
23. Moore, R. L., Sterling, A. C. & Falconer, D. A. Magnetic untwisting in solar jets that go into the outer corona in polar coronal holes. *Astrophys. J.* **806**, 11 (2015).
24. DeVore, C. R. & Antiochos, S. K. Homologous confined filament eruptions via magnetic breakout. *Astrophys. J.* **680**, 740-756 (2008).
25. Shibata, K. *et al.* Chromospheric anemone jets as evidence of ubiquitous reconnection. *Science* **318**, 1591-1594 (2007).
26. De Pontieu, B. *et al.* The origins of hot plasma in the solar corona. *Science* **331**, 55-58 (2011).
27. Ellerman, F. Solar hydrogen "bombs". *Astrophys. J.* **46**, 298-300 (1917).
28. Vissers, G. J. M., van der Voort, L. & Rutten, R. J. Ellerman bombs at high resolution. II. Triggering, visibility, and effect on upper atmosphere. *Astrophys. J.* **774**, 32 (2013).

Acknowledgements. P.F.W. was supported by a Royal Astronomical Society Fellowship at Durham University and previously by a NASA Postdoctoral Program Fellowship at NASA Goddard Space Flight Center. S.K.A. and C.R.D. were supported by NASA Living With a Star and Heliophysics Supporting Research grants. The numerical simulations were supported by NASA High-End Computing allocations to C.R.D. on discover at NASA's Center for Climate Simulation.

Author Contributions. P.F.W. designed and performed the numerical simulations, created the graphical outputs, and drafted the manuscript. S.K.A. conceived the investigation, consulted on the simulations, and revised the manuscript. C.R.D. developed the numerical model, assisted in designing the experiments, acquired the computer resources required, and revised the manuscript.

Author Information. The authors declare no competing financial interests. Correspondence should be addressed to P.F.W. (peter.f.wyper@durham.ac.uk).

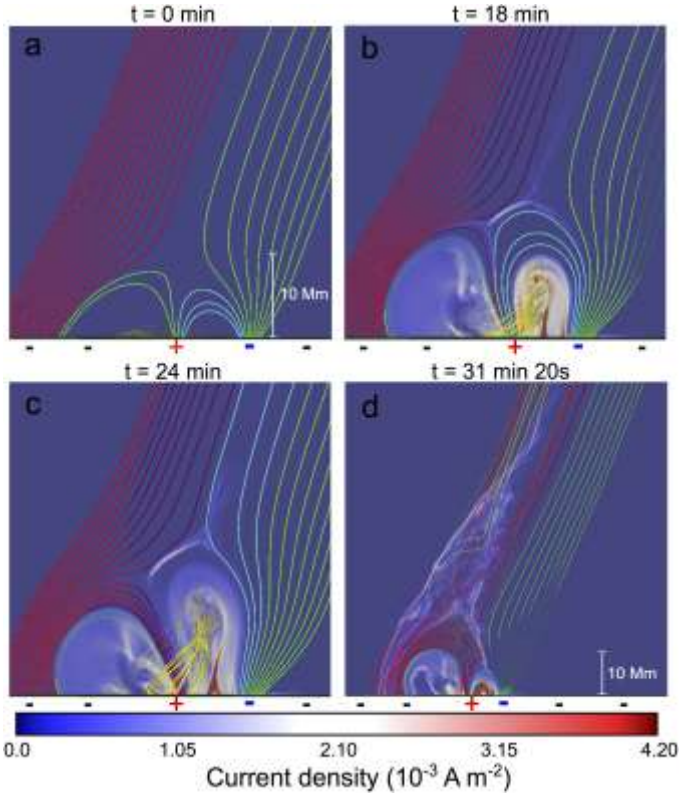

Figure 1. The simulated mini-filament jet evolution. Red/blue +/− signs show the bipole position, black − signs the background field. Field lines are coloured to depict the various magnetic field regions (compare with Figure 4): the filament/flux-rope structure (yellow; b,c) forms beneath the central arcade (blue; a,b) before erupting (d). Semi-transparent shading shows current density in the plane. The high value in the thin strip at the null (b,c) depicts the breakout current sheet. The flare current sheet is short when it first forms below the slowly rising flux rope (c), but elongates vertically and strengthens substantially as the flux rope accelerates (d).

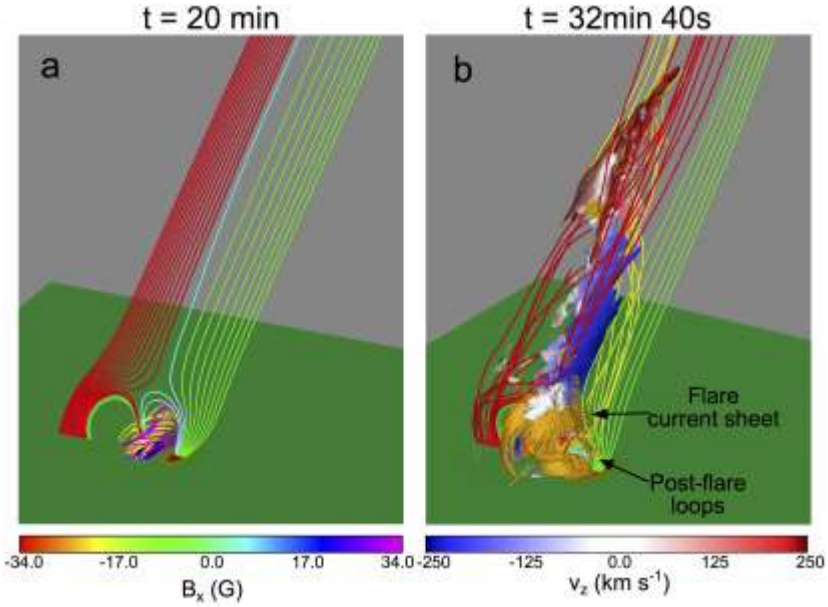

Figure 2. 3D structure of the filament field and the jet. Bottom plane is shaded according to vertical magnetic field B_x. Isosurfaces show current density ($|J| = 1.8\times10^{-3}$ A m^{-2}; orange) and velocity magnitude ($|\mathbf{v}| = 250$ km s^{-1}; red/blue colour-shading denotes the untwisting horizontal component, v_z, on this iso-surface.).

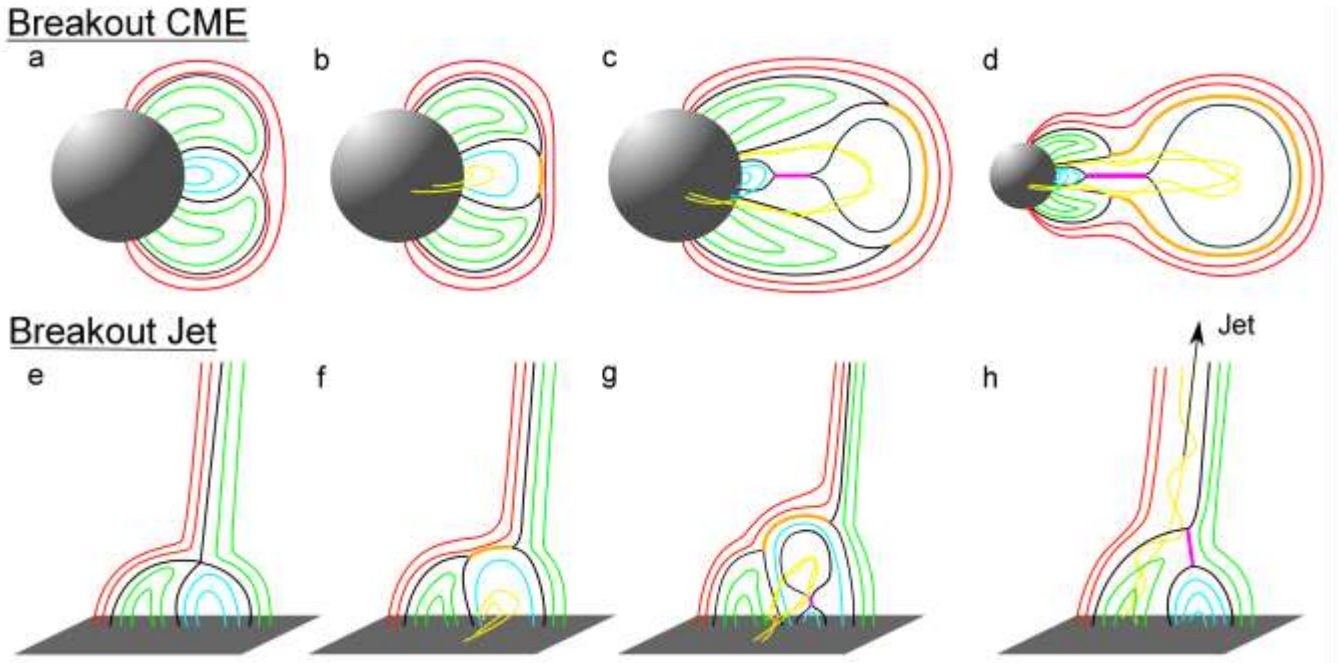

Figure 3. Schematic of the breakout process. Top panels: in CMEs, bottom panels: in jets. Black field lines show separatrices (or quasi-separatrices) dividing different regions of the magnetic field (red, green, blue). Yellow field lines show the core of the filament/flux rope. Orange shading denotes the breakout current sheet, pink shading the flare current sheet.

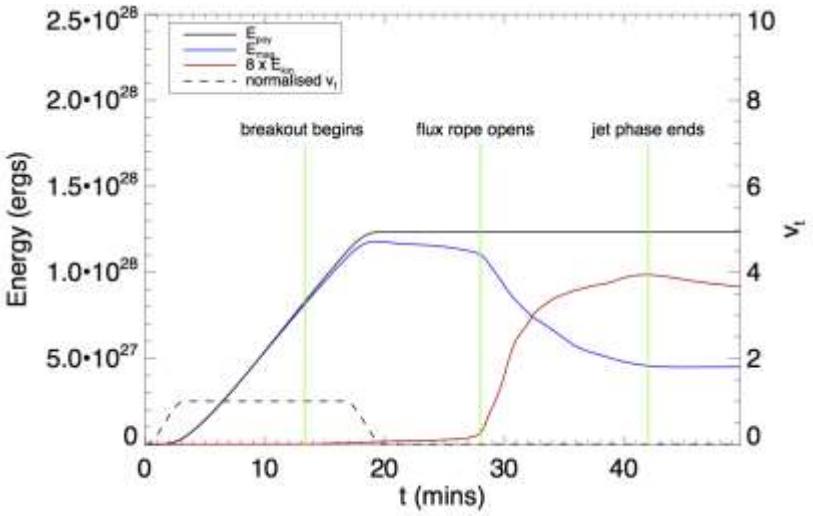

Figure 4. Energy stored and released during the simulation. Magnetic energy injected as cumulative Poynting flux, E_{poy} (black solid); free magnetic energy stored in the volume, E_{mag} (blue); and kinetic energy of plasma motion, E_{kin} (red). The time profile of the driver normalised by the maximum driving speed (black dashed) and key transition times in the simulation (green) also are shown.

METHODS

Numerical experiment details.

The simulation was conducted using the Adaptively Refined Magnetohydrodynamics Solver (ARMS), to solve the ideal magnetohydrodynamic equations on an adaptively refined grid. Reconnection occurs through numerical diffusion, and an adiabatic energy equation is used in the manner of our previous calculations[15,16]. The energy equation employed in our simulation captures heating/cooling from compression/expansion. However, heating from ohmic and viscous dissipation, cooling from radiative losses, and energy transfer by thermal conduction are not. As the dynamics are magnetic dominated, due to the low thermal pressure and plasma beta, we expect that their inclusion would produce local differences in plasma temperature and density, but that the plasma dynamics would not change very much. We also expect that the general evolution of magnetic and kinetic energies would be largely unchanged, although the precise values would certainly very somewhat due to the competing effects of the additional sources/sinks in energy.

The initial potential magnetic field of the simulation consists of a uniform background field of −2 G inclined 22° to the vertical, superimposed upon a set of 16 (8 positive and 8 negative) sub-photospheric dipoles aligned vertically and arranged to yield strong positive and negative polarity patches on the photosphere typical of emerged bipolar regions. The combined strengths of the various dipoles and background field give peak vertical field strengths in the positive and negative patches of 34 G. The atmosphere consists of uniform plasma at a temperature of 1.2 MK and density of 4×10^{-16} g cm^{-3}. In the corona, the plasma beta (ratio of thermal to magnetic pressure) is well below unity, so the dynamics are dominated by magnetic forces. In our simulation, the beta is 2×10^{-1} in the background field and drops to 9×10^{-4} in the center of strong-field patch of the bipole on the photosphere (situated at $x = 0$). The driving on the photosphere is the same form used in our previous calculations[15,16] and follows the contours of the vertical field component at the photosphere. This maintains the initial potential field as the lowest-energy state throughout the simulation, so any change in the magnetic energy represents stored free energy. The peak driving speed is 25 km s^{-1}, which is faster than typically inferred flow speeds on the solar surface[29] but still significantly slower than the local Alfvén (4850 km s^{-1}) and sound (130 km s^{-1}) speeds. Thus, the system evolves quasi-statically until the internal dynamics become fast. The driving is ramped up, held constant for a time, and then is ramped back down to zero over a period of 20 minutes (Figure 4). There is a small overlap of the driving interval with the onset of the breakout reconnection; however, the driving has long ceased when the flux rope opens and the jet is launched at time 28 minutes. The numerical domain has dimensions [600 Mm, 600 Mm, 200 Mm], large enough that the jet does not reach the boundary before the simulation is halted. The numerical grid adapts according to criteria[21] that refine the grid in regions of medium- to high-strength current and de-refine otherwise (Extended Data Figure 3). We used 6 levels of refinement in this simulation. The resolution necessary for an equivalent fixed-grid calculation would be 4608×4608×1536, making this by far the highest resolution 3D calculation of its type to date.

Flux-rope rise-speed calculation. The rise speed of the flux rope during the breakout-reconnection phase was calculated by inspecting contour plots of current density in the plane ($z = 0$) that the flux rope crosses perpendicularly. The center of the flux rope was estimated by eye as the center of the circular current region that forms above the PIL of the bipole

(Extended Data Figure 1a). For each frame until the flux rope opened, this procedure was repeated; the rise speed then was calculated from the rate of change of the center position (Extended Data Figure 1b). We stopped tracking the flux rope shortly before its reconnection with the open field. After this time the axis of the rope aligns with the ambient field and the speed of the filament plasma cannot be estimated with this method. Supplementary Video 4 shows a video of Extended Data Figure 1a, depicting the movement of the tracked position with time.

Code Availability. We have opted not to make ARMS available due to its complexity, which demands expert assistance to set up, run, and analyze simulations, and to its continually being improved and extended, which require frequent software updates. Interested parties are invited to contact the authors for more detailed information.

Data Availability. The 3D simulation data generated and analyzed for this paper occupy approximately 200GB of disk space. Interested parties are invited to contact the authors to make arrangements for the transfer of those data. The 1D reduced data plotted in the figures are provided with the paper as MS Excel spreadsheets.

29. Brandt, P. N. *et al.* Vortex flow in the solar photosphere. *Nature* **335**, 238-240 (1988).

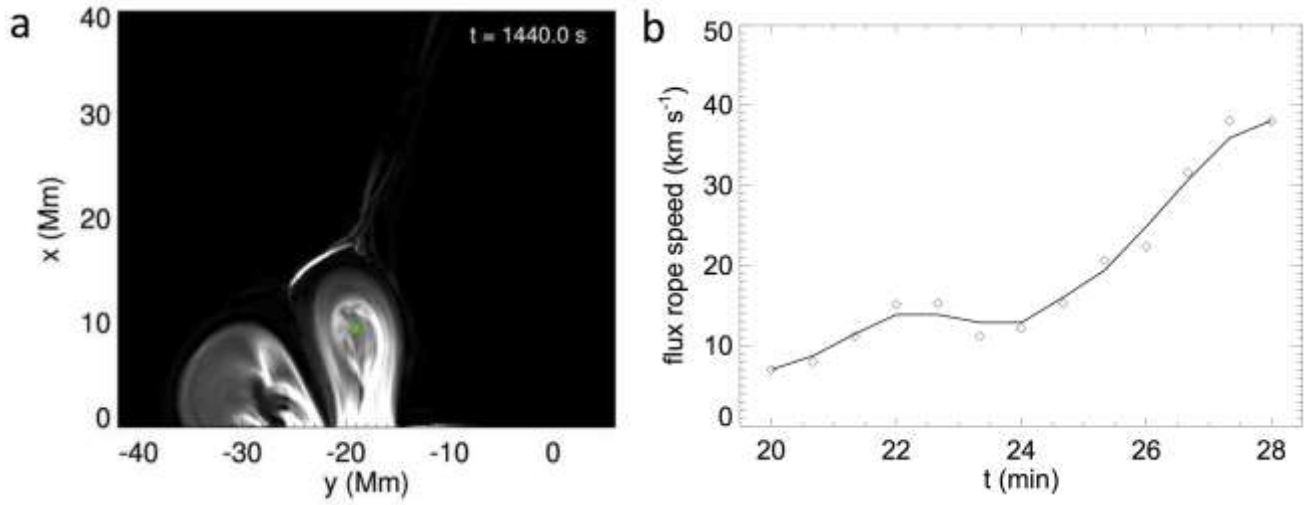

Extended Data Figure 1. Estimate of the speed of the flux rope during the slow-rise phase. (a) Current density in the mid-plane (saturated at 6×10^{-3} A m^{-2}). The green dot shows the position near the center of the flux rope that is tracked in time. (b) Inferred speed of the flux rope axis (diamonds); the solid line shows these data after applying a two-point boxcar smoothing.

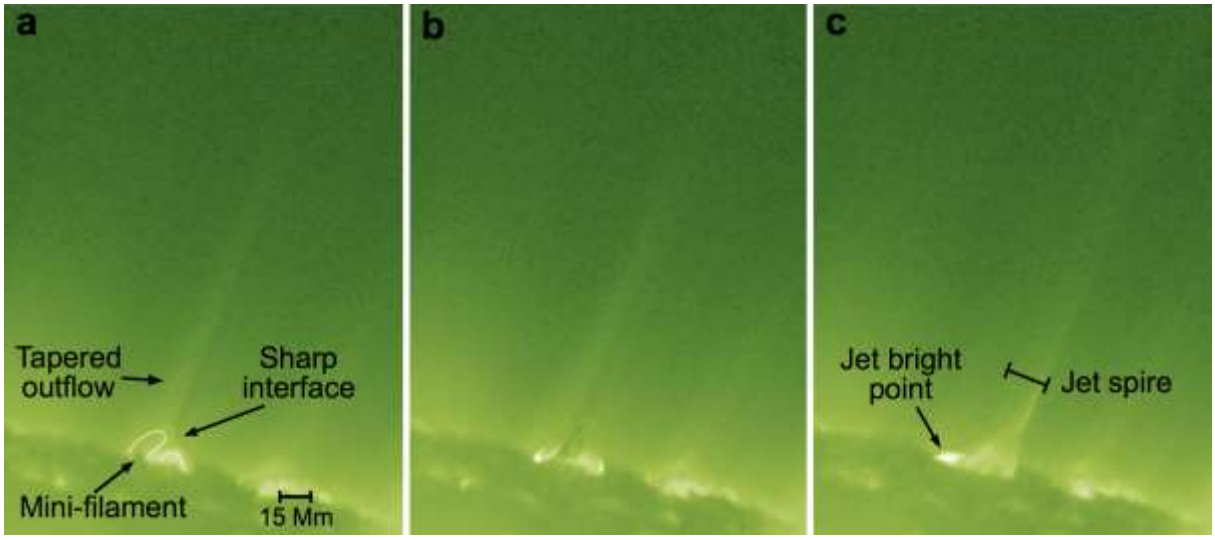

Extended Data Figure 2. Mini-filament jet example. A large coronal jet produced in conjunction with the eruption of a mini-filament[23] as seen in images from SDO/AIA Fe XII 193Å. The inferred coronal loop structure is depicted in white in (a).

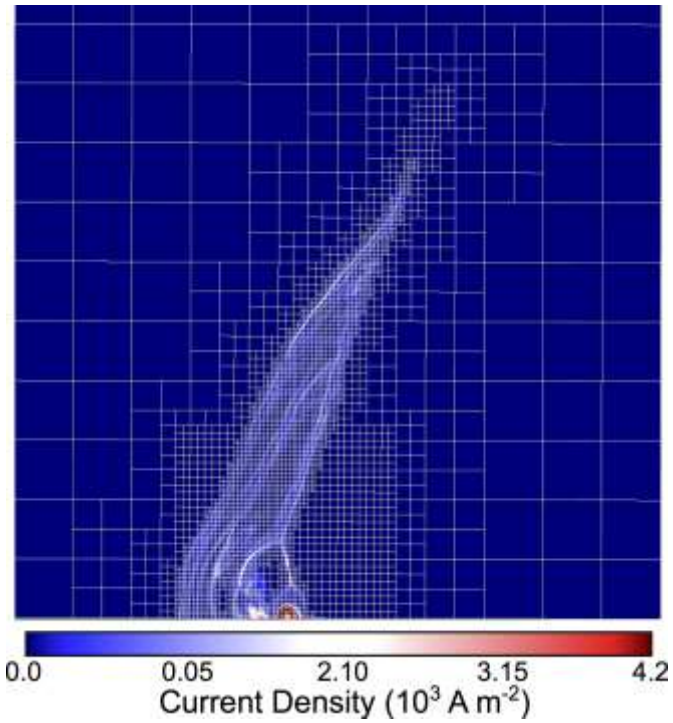

Extended Data Figure 3. The block-adapted mesh during the jet. In the z = 0 plane at t = 32 mins 40s. Each box corresponds to a block of 8×8×8 cells. Grid parameters are chosen to refine in regions of medium to high current density, shown as regions of white and red. The grid increases in size by a factor of 4 during the simulation, and the minimum resolution is 104 km.

Supplementary Video 1: The simulated mini-filament jet evolution. See Figure 2 legend and text for descriptions of the evolution and field lines/shading depicted.

Supplementary Video 2: 3D visualisation of the jet. See Figure 3 legend and text for descriptions of the evolution and field lines/iso-surfaces depicted.

Supplementary Video 3: Mini-filament jet example. See Extended Data Figure 2 legend and text for description.

Supplementary Video 4: Evolution of the flux rope during the slow rise phase. See Extended Data Figure 1 and methods section for descriptions of the shading a method for following the flux rope.